Identification and Analysis of Deformation Areas in the Construction Stage of Pumped Storage Power Station Using GB-InSAR Technology

Honglei Yang ⬛, Youfeng Liu ⬛, Hongdong Fan ⬛, Xiaoliang Li, Yuhan Su ⬛, Xu Ma, and Liuyu Wang ⬛

Abstract—To meet the needs of the rapid development of new energy sources, China is currently accelerating the construction of pumped storage power stations (PSPS). However, the complex geological environment and large-scale construction can easily cause deformation areas, such as collapse and sliding, on the surface of PSPS. This article adopts ground-based interferometric synthetic aperture radar (GB-InSAR) technology to monitor surface deformation using 206 ground-based radar (GBR) data collected from 2022/07/31 10:24 to 2022/08/06 14:57 with a PSPS in the construction stage in western China. In the selection of permanent scatterers (PSs) for GBR data processing, statistical homogeneous pixels (SHPs) information is considered in this article. Based on the fast SHP selection (FaSHPS) algorithm, we introduce intensity deviations (D_I) to exclude pixels with unstable intensity performance in the temporal dimension and propose the $D_I + FaSHPS$ algorithm, which is experimentally proven to have higher SHPs selection accuracy and computational efficiency. By combining with the traditional PSs selection algorithm, the distribution density of monitoring points is effectively improved. In addition, based on the deformation results and on-site survey, this article analyzes and discusses the identified deformation areas in detail from the aspects of natural geography and man-made activities. The results show that the surface is relatively stable overall, except for the effects of man-made activities. This study has demonstrated the remarkable reliability and superiority of the GB-InSAR technology in identifying and analyzing deformation areas in the construction stage of PSPS.

Index Terms—Deformation areas, ground-based interferometric synthetic aperture radar (GB-InSAR), pumped storage power station (PSPS), permanent scatterers (PSs) selection, statistical homogeneous pixels (SHPs).

Honglei Yang, Youfeng Liu, Yuhan Su, and Xu Ma are with the School of Land Science and Technology, China University of Geosciences, Beijing 100083, China (e-mail: hongleiyang@cugb.edu.cn; jasonliuyf@163.com; s_yuhan@163.com; 1159396104@qq.com).

Hongdong Fan is with the Jiangsu Key Laboratory of Resources and Environmental Information Engineering, China University of Mining and Technology, Xuzhou 221116, China (e-mail: cumtfanhd@163.com).

Xiaoliang Li is with the Beijing Institute of Surveying and Mapping, Beijing 100038, China (e-mail: nvt616@126.com).

Liuyu Wang is with the Jiangsu Provincial Hydraulic Research Institute, Nanjing 210017, China (e-mail: wangly@cumt.edu.cn).

I. INTRODUCTION

A PUMPED storage power station (PSPS) uses electrical energy from the low power load to pump water to the upper reservoir and then releases water to the lower reservoir to generate electricity during peak power load periods [1], [2]. Due to its role in grid peak regulation, voltage regulation, energy storage, and power stability control, PSPS have become an important type of hydropower projects around the world [3]. With some of the world's richest water resources, PSPS construction in China has been growing rapidly since 1968. Entering a new era, China has solemnly announced to the world that it aims to achieve "peak carbon emission" by 2030 and "carbon neutrality" by 2060. As a renewable and clean energy, the construction scale of PSPS will undoubtedly continue to increase [4]. The monitoring object is the first PSPS project in western China, which started construction in 2016. After the project is put into operation, it will be able to achieve joint and coordinated operation with thermal power, wind power, and solar power generation in Northwest China, playing an important role in achieving the "double carbon" goal.

Traditional means of deformation monitoring (e.g., level, total station, navigation, and positioning equipment) are limited to a small number of ground points and require manual operation or on-site deployment of instruments, with strict requirements for the terrain environment [5], [6]. 3-D laser scanning technology captures dense, irregular data, requiring larger data storage space and longer data processing times [7]. The main advantage of space-borne interferometric synthetic aperture radar (InSAR) systems is its wide spatial coverage, which is suitable for surface deformation monitoring in large study areas, such as cities, large slopes, and mining areas [8], [9], [10], [11]. However, the limitations of fixed orbit, long revisit time, low data resolution, and insensitivity to deformation in the north–south direction have hindered the wide application of space-borne InSAR systems in site-specific deformation monitoring. Compared with space-borne InSAR systems, ground-based (GB) InSAR systems can be deployed near the monitoring target and can also adjust the imaging period and observation direction, with higher data resolution, and their flexibility is a significant advantage in deformation monitoring [12], [13]. GB-InSAR systems have been developed over two decades, and they mainly consist of the following two types: synthetic

aperture radar (e.g., IBIS [14], FastGBSAR [15]) and real aperture radar (e.g., gamma portable radar interferometer, GPRI and GPRI-II [16]). In addition, GB-InSAR technology can measure the position changes of various natural objects [17], [18], [19], [20] such as slopes, mining areas, mountains and glaciers, as well as large buildings [21], [22], [23], such as bridges, dams, tall buildings, and hydropower stations with submillimeter accuracy.

Currently, the most commonly used data processing method for GB-InSAR technology is multi-temporal InSAR (MT-InSAR) [24], which mainly includes persistent scatterer InSAR (PS-InSAR) [25] and small baseline subset [26]. MT-InSAR can more accurately obtain the surface deformation rate and time series by modeling and analyzing the selected reflection phase stabilization points [27], [28], [29]. Coherence point selection plays a very important role in MT-InSAR, and its quality and density directly affect the extraction accuracy of deformation parameters [30], [31]. Generally, amplitude deviation index and coherence threshold are used as the selection criteria to select high-quality permanent scatterers (PSs) [32]. PSs return significantly more energy than other scatterers within a resolution pixel, thus reducing the decorrelation. Subsequently, the SqueeSAR method, which aims to improve the distribution density of monitoring points, has been proposed to accompany the increased demands of surface deformation monitoring [33]. This second generation PS-InSAR method uses the temporal amplitude values of two pixels within a window to construct a probabilistic distribution to identify statistically homogeneous pixels (SHPs). With the continuous emergence of algorithms for SHPs selection, the accuracy of its selection has been greatly improved [34], [35], [36]. In addition, as an important way to select PSs, SHPs effectively enriches the content of GB-InSAR technology [37].

In reality, the natural geological and geomorphological conditions of PSPS projects are often bad, with high and steep banks and complex topography and dense vegetation [38]. It is difficult to select a sufficient number of monitoring points for surface deformation analysis in such areas. In addition, geological hazards, such as slope failures and surface landslides, occasionally occur during the construction process, requiring timely, flexible safety monitoring of hazard areas. Furthermore, the identification and analysis of deformation areas during the construction stage of a PSPS require a large scanning angle (>180°) to obtain the wide area surface deformation information. Unfortunately, there is not much research related to GB-InSAR technology for such monitoring situations. In the face of the above predicament, this article has carried on the exploration and research full of practical significance. The rest of this article is organized as follows. First, this article presents an overview of the study area as well as the experimental design and data in Section II. Then, the article elaborates the MT-InSAR method in detail and focuses on the PSs selection method based on SHPs information in Section III. Subsequently, according to the PSs selection and deformation monitoring results, this article presents a detailed analysis and discussion in Section IV. Finally, Section V concludes this article..

II. STUDY AREA AND EXPERIMENTS

A. Study Area

The PSPS studied in this article is located in the western region of China, approximately 128 km from downtown Xi'an in Shaanxi Province [39]. The study area is located at the eastern foot of the Taibai Mountains, the main peak of the Eastern Qinling Mountains, and is a medium-high mountainous area, adjacent to the Weihe Plain in the north, with a north–south tilted fault block structure. The study area is characterized by high mountains and deep ravines, dense vegetation, and complex topography. When fully completed, the PSPS will mainly serve the Shaanxi Power Grid, undertaking tasks such as peak regulation, valley filling, frequency modulation, and emergency backup. The entire PSPS project is mainly composed of upper reservoir, lower reservoir, water transmission system, underground plant, and switching station, while this study only includes the upper reservoir area of the PSPS [see Fig. 1(a)]. Among them, the normal storage level of the upper reservoir is 1392 m, with a corresponding storage capacity of 8.96 million m^3, the dead water level is 1367 m, with a dead storage capacity of 460 000 m^3, and the effective storage capacity is 8.5 million m^3. The upper reservoir dam is a concrete panel rockfill dam with a maximum height of 125.90 m, and the elevation and length of the dam crest are 1396 m and 363 m, respectively. At dawn on 31 July 2022, a localized collapse occurred on the south side of the upper reservoir bank. Fortunately, there was no damage to people or equipment, but there is an urgent need for deformation monitoring of the collapse and its surrounding area to assess its surface stability.

B. Experiment Design

1) Site Selection for Instrument Installation: In order to monitor the deformation of the upper reservoir and especially the collapse area, it is fundamental to ensure that the data acquisition is through-viewed and the instrument installation is stable. The location of the instrument needs to meet the following conditions:

1) no obstacles on the ground affecting the installation and operation of the instrument, with a clear view;
2) avoid areas subject to ground vibrations from site construction;
3) avoid areas with unstable geological structures;
4) avoid areas susceptible to flooding or large changes in the water table;
5) keep the station as close to the surrounding atmosphere as possible to reduce the impact of atmospheric errors.

As this is a short-term rapid monitoring, there is no need to build a fixed monitoring pier, i.e., the tripod is screwed to the ground for instrument installation. We organized a professional team to conduct a site survey and completed the site selection [see Fig. 1(a)] and instrument installation [see Fig. 1(b)] based on the actual site environment and installation requirements.

2) Data Acquisition Settings: The GPRI-II instrument with 360° rotational monitoring capability was chosen to meet the
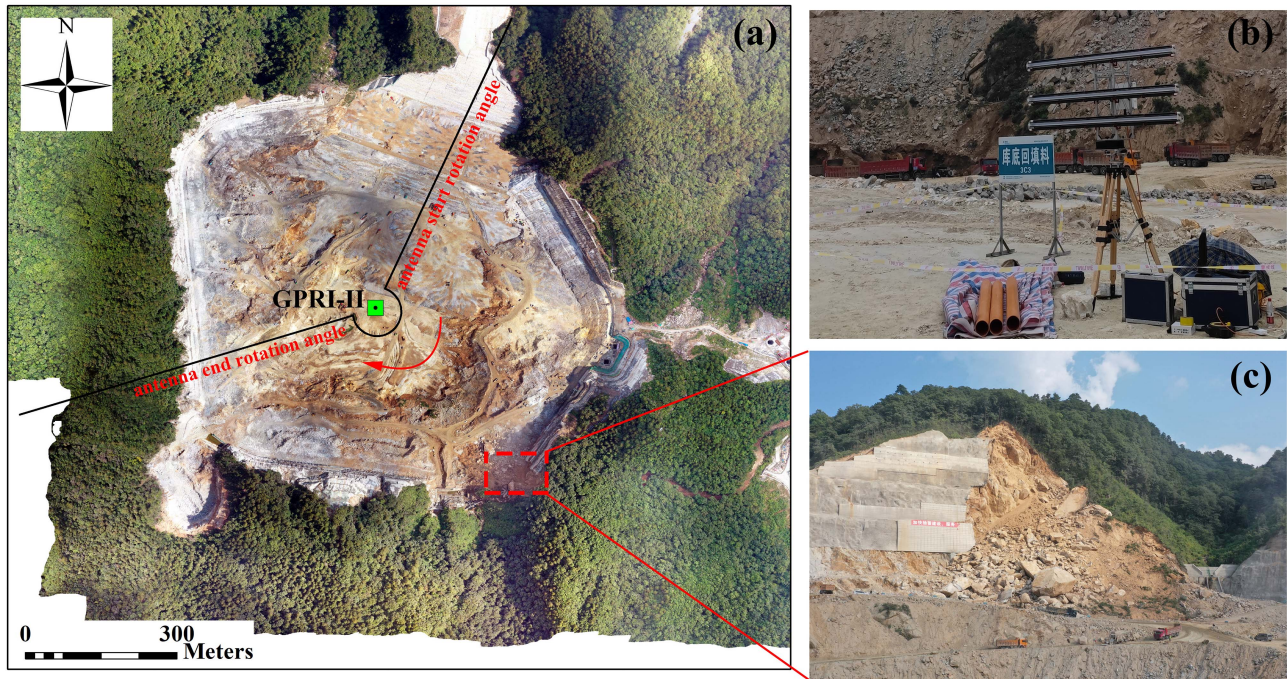
Fig. 1. Detailed depiction of the study area. (a) Scope of the study area. (b) Installation of GPRI-II instrument. (c) Optical image of the collapse area.

TABLE I
MEASUREMENT PARAMETERS DURING SAR DATA ACQUISITION

Parameter	Value
Center frequency	17.2 GHz
Antenna elevation angle	15°
Receiver gain	18 dB
Measuring distance range	50m-1000m
Antenna rotation angle range	-80°- 150°
Range resolution	0.75m
Azimuth resolution (at 1 km)	6.72m
Data acquisition interval	10min

needs of the monitoring range. Before formal monitoring, 1–3 images are first acquired quickly for inspection and their radar intensity should be clear on target and less than 60% of points less than 25 dB. Then, the measurement parameters are adjusted in time according to the quality of the data. The specific measurement parameters for the acquisition of radar data are given in Table I.

C. Experimental Data

Considering the harsh site environment of the upper reservoir, which is under construction, it is difficult to guarantee the absolute safety of instruments and personnel when conducting continuous monitoring for long periods of time. Therefore, from 31 July 2022 onwards, radar data collection will only be carried out during daytime hours. At the same time of radar data collection, professional engineers carried out field investigation, always paying attention to the surface morphology of the reservoir bank, and no obvious collapse and slip area was found again. In order not to interfere with the normal construction schedule of the PSPS, the radar data collection work was completed on August

6, 2022. A total of 227 images of GBR data were acquired. The quality of each image was assessed visually and then images with severe noise effects such as atmospheric and ambient noise were removed, resulting in a final selection of 206 images for subsequent data processing (see Table II). The image acquired near the center of the temporal baseline at 2022/08/03 12:23 was used as the master image and the remaining slave images were registered.

In the polar coordinate system, the intensity map generated by the master image is shown in Fig. 2(a), and the average intensity map generated by 206 temporal radar images after registration is shown in Fig. 2(b). Fig. 2(a) shows a clear image with less noise influence, indicating a high quality of data collection; Fig. 2(b) contains some noise signals, indicating that the data acquisition process is inevitably interfered by the complex surrounding environment but the overall image quality is satisfactory. In summary, the collected temporal radar data can meet the requirements of subsequent data processing and deformation inversion. In addition, we also used UAV survey technology to conduct field verification and auxiliary analysis of the study area, and generated digital surface model (DSM) and digital orthophoto maps (DOM) according to the aerial photographs. DSM is used to geocode radar data; DOM is mainly used for visual analysis of the study area.

III. METHODS

The GBR data in this article is Ku band, which has a short wavelength and is susceptible to spatial and temporal decoherence. Therefore, we chose the most suitable MT-InSAR method [25]. The MT-InSAR first generates a multimaster interferogram stack from adjacent radar data to reduce the effects of temporal

TABLE II
DATA ACQUISITION FROM JULY 31 TO AUGUST 6, 2022

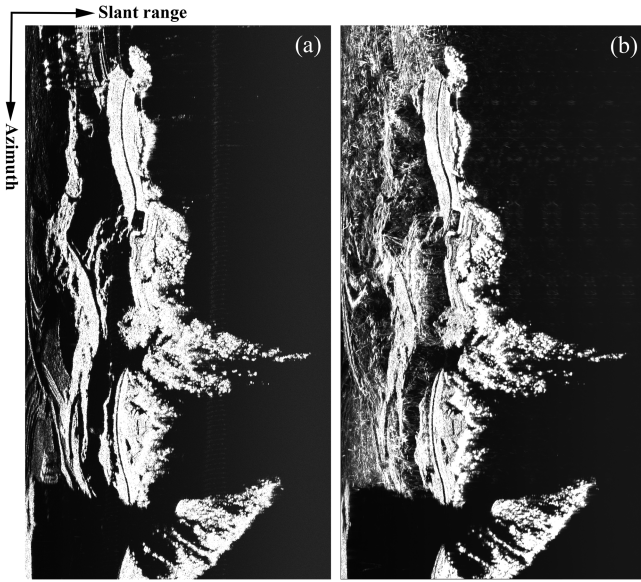| NO.	Starting time	End time	Number of images
1	2022/07/31 10:24	2022/07/31 16:04	32
2	2022/08/01 10:56	2022/08/01 16:16	31
3	2022/08/02 09:37	2022/08/02 16:07	35
4	2022/08/03 10:42	2022/08/03 15:43	23
5	2022/08/04 10:43	2022/08/04 15:13	27
6	2022/08/05 09:03	2022/08/05 15:02	26
7	2022/08/06 09:37	2022/08/06 14:57	32

Fig. 2. Intensity map of GBR data in polar coordinate system. (a) Master image intensity map. (b) Average intensity map.

Fig. 3. Data processing workflow of MT-InSAR.

decoherence and atmospheric noise, then selects PSs based on the inverse of the amplitude deviation and the temporal coherence threshold, filters the interferometric phase corresponding to the PSs to remove atmospheric and noisy phases, and finally performs phase unwrapping to reconstruct the line-of-sight (LOS) directional deformation rate and temporal deformation based on minimum norm theory (see Section III-A). Uniquely in this article, the spatial homogeneity characteristics of the pixels are also taken into account when selecting the PSs, that is, PSs are selected based on the SHPs selected from the temporal amplitude values of the GBR data (see Section III-B).

A. MT-InSAR

The data processing workflow of MT-InSAR is shown in Fig. 3. Considering the short sampling interval of the 206 GBR data and the small variation of the atmosphere in a short period of time, this article generates multimaster interferometric stacks with the interval between two adjacent images as the temporal baseline threshold and also ensures redundant observations. In the end, a total of 409 interferometric stacks are generated. In addition, when the GB-InSAR system conducts deformation monitoring, the radar center position is fixed, so the spatial baseline is almost zero, and the baseline error can be ignored. Assuming, N radar data generates M wrapping interferograms,
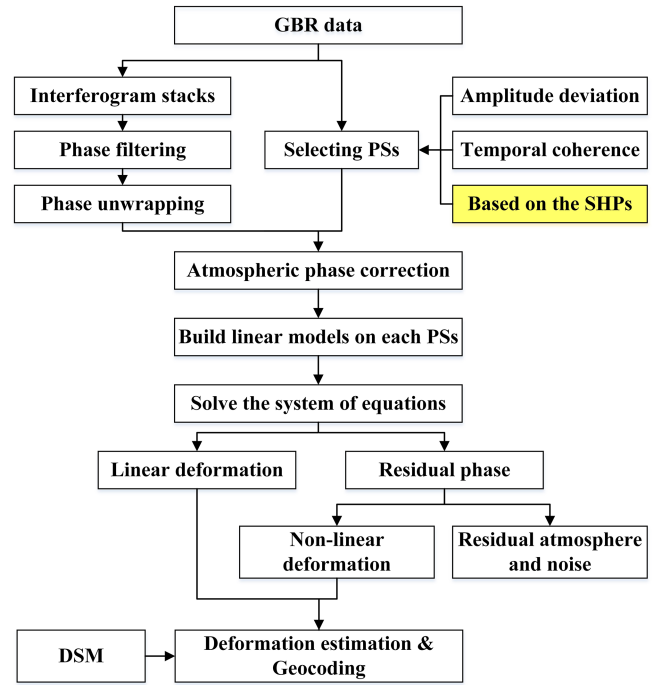
the unwrapping phase of the ith wrapping interferogram is expressed as [13]

$$\Phi^i = \varphi^i_{\text{def}} + \varphi^i_{\text{atm}} + \varphi^i_{\text{noi}} + 2k\pi \tag{1}$$

where $\varphi_{\text{def}}, \varphi_{\text{atm}}, \varphi_{\text{noi}}$ are the deformation phase, the atmospheric phase, and the noise phase, respectively; k is the ambiguity of the whole cycle. While generating the interferogram stack, PSs need to be selected where the radar scattering characteristics remain stable over the time series. In the classical PS-InSAR method, Ferretti et al. [25] use information on the amplitude deviation of the pixels in the temporal radar data to select the PSs. The amplitude deviation D_A means by calculating the amplitude mean m_A and standard deviation σ_A for each pixel, which is expressed as

$$D_A = \frac{\sigma_A}{m_A}. \tag{2}$$

The smaller the amplitude deviation, the more stable the amplitude information. The amplitude deviation only uses the amplitude information of the pixel, which has the advantages of small calculation and easy extraction. Another way of selecting PSs is based on the average coherence of the interferogram stack
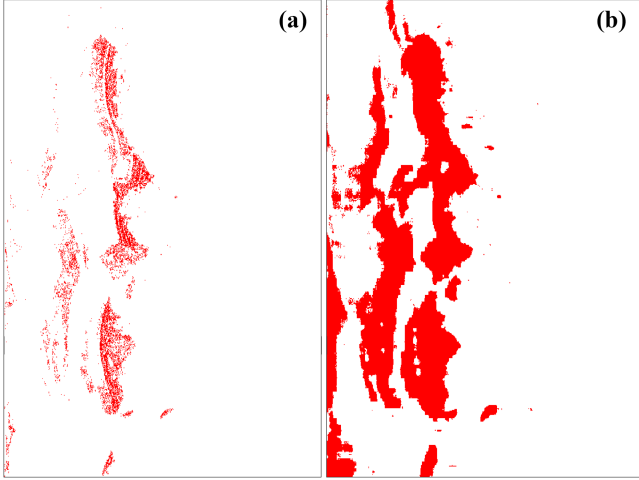
Fig. 4. PSs selection results. (a) Inverse of the amplitude deviation. (b) Temporal coherence mean.

[40], [41]. The coherence of all pixels (x, y) in each interferogram needs to be calculated as follows:

$$\gamma = \frac{\left| \sum_{x=1}^{I} \sum_{y=1}^{J} m(x,y) s^*(x,y) \right|}{\sqrt{\sum_{x=1}^{I} \sum_{y=1}^{J} |m(x,y)|^2 \sum_{x=1}^{I} \sum_{y=1}^{J} |s(x,y)|^2}} \quad (3)$$

where I, J are the sliding neighborhood window sizes, respectively; m, s are the master and slave images, respectively; and $*$ represents the complex conjugate.

The mean $\bar{\gamma}$ is then calculated from the temporal coherence value γ, and a suitable threshold is set to select the PSs. The higher the mean value of the temporal coherence, the more stable the radar scattering characteristics and the less the ground features are disturbed by noise. To maintain uniformity with the professional GAMMA software, PSs were selected in this article based on the inverse of the amplitude deviation. The threshold value was set to 1.5, and a total of 76 269 PSs were selected, as shown in Fig. 4(a). The threshold value of the temporal coherence mean $\bar{\gamma}$ was set to 0.8 and a total of 499 478 PSs were selected, as shown in Fig. 4(b). Generally, the PSs selected by the two methods are combined together for subsequent processing.

Commonly, the sum of the segmental linear deformations is used to represent the deformation values over the entire monitoring time. The deformation phase corresponding to PS (x, y) in the ith wrapping interferogram is

$$\varphi_{\text{def},x,y}^i = -\frac{4\pi}{\lambda} \Delta r_{x,y}^i = -\frac{4\pi}{\lambda} \sum_{j=s_{i+1}}^{m_i} (t_j - t_{j-1}) v_j. \quad (4)$$

Considering that the study area has a wide range of observations and significant height variations, the atmospheric phase is corrected by a linear regression model related to slant range and height. If (x', y') is set as the reference point, the atmospheric phase can be expressed as

$$\varphi_{\text{atm},x,y}^i = a_0 + a_1 * r + a_2 * r * \Delta h_{x,y,x',y'} \quad (5)$$

where a_0, a_1, a_2 are coefficients; r is the slant range between the radar and the point target; and $\Delta h_{x,y,x',y'}$ is the height difference between the point target and the reference point. The noise phase can be removed by filtering in both the spatial and temporal dimensions. After removing the atmospheric and noise phases, the differential phase between each PS pixel and the reference pixel is expressed as

$$\Delta \Phi_{x,y,x',y'}^i = -\frac{4\pi}{\lambda} \sum_{j=s_{i+1}}^{m_i} (t_j - t_{j-1}) v_j + \omega_{x,y,x',y'}^i \quad (6)$$

$$v^T = \left[v_1 = \frac{\varphi_2}{t_2 - t_1}, \ldots, v_{N-1} = \frac{\varphi_N - \varphi_{N-1}}{t_N - t_{N-1}} \right]. \quad (7)$$

According to (6) and (7), the deformation phase is a linear deformation, which is expressed as

$$\sum (t_{i-1} - t_i) v_i = \Delta \varphi_j, \quad j = 1, \ldots, M. \quad (8)$$

The matrix form is

$$Av = \Delta \varphi \quad (9)$$

where A is an $M \times N$ matrix. Singular value decomposition A can get the least squares solution in the sense of the minimum norm, and then the deformation phase of the model can be obtained [42]. $\omega_{x,y,x',y'}^i$ in (6) is the residual phase, which includes atmospheric residual, nonlinear deformation, and noise. Atmospheric residual and noise can be removed by the filtering method. Then, the nonlinear deformation in the residual phase is summed with the linear deformation to obtain the total deformation of all PSs. Finally, the cumulative deformation is obtained by converting the interferogram stack into single master image form by least squares.

B. PSs Selection of SHPs

According to the above mentioned, we generally select PSs based on indicators such as amplitude deviation and temporal coherence. However, this traditional selection method only takes into account the temporal dimension of the radar data and does not make sufficient use of the spatial relationships between the pixels. Moreover, as the monitoring period grows, the temporal coherence decreases and so does the PSs density. Thus, this article incorporates content of the SHPs from the SqueenSAR method in the selection of the PSs and enhances it slightly [33]. Currently, the algorithms selected for SHPs are mainly classified into nonparametric statistical algorithms and parametric statistical algorithms. In this article, the algorithms in each class that are widely used and have high accuracy are separately experimented in the study area. In this article, the algorithms that are widely used and with high accuracy in each category are tested in the study area respectively.

The BWS test is one of the typical representatives of the nonparametric statistical algorithm, the basic idea of which is to weight the squared values of the empirical distribution differences [43]. It is assumed that statistical calculations are performed on reference pixel B_{ref} and neighborhood pixel B_{neig}

in the temporal radar data, namely, as follows:

$$B_{\text{ref}} = \frac{1}{2N^2} \sum_{i=1}^{n} \frac{(R_i - 2i)^2}{\frac{i}{N+1} \cdot \left(1 - \frac{i}{N+1}\right)}$$

$$B_{\text{neig}} = \frac{1}{2N^2} \sum_{i=1}^{n} \frac{(H_i - 2i)^2}{\frac{i}{N+1} \cdot \left(1 - \frac{i}{N+1}\right)}$$

$$B = \frac{1}{2} \left(B_{\text{ref}} + B_{\text{neig}}\right) \qquad (10)$$

where R_i and H_i are the rank of the reference pixel sample and the neighborhood pixel sample, respectively. In addition, the parametric statistical algorithm represented by fast SHP selection (FaSHPS) is also widely used [34]. The core principle of the FaSHPS is to transform the hypothesis testing problem into confidence interval estimation. The SHPs of the reference pixel are determined based on their similarity to neighborhood pixels in the time series. When a confidence interval is constructed at a given confidence level $1 - \alpha$, all values within the interval are considered as plausible values for the unknown parameter while values outside the interval are discarded. According to the central limit theorem, with the increase of radar data N, the average amplitude $\bar{A}(p)$ of pixel p is closer to the normal distribution, namely: $\bar{A}(p) \sim N(\mu(p), Var(A(p))/N)$. The interval estimate for $\bar{A}(p)$ is

$$P\left\{\mu(p) - z_{1-\alpha/2} \cdot \sqrt{\frac{\text{Var}(A(p))}{N}} < \bar{A}(p) < \mu(p) \right.$$

$$\left. + z_{1-\alpha/2} \cdot \sqrt{\frac{\text{Var}(A(p))}{N}} \right\} = 1 - \alpha \qquad (11)$$

where $P\{\cdot\}$ is the probability, $z_{1-\alpha/2}$ is the quantile at confidence level $1 - \alpha$, $\mu(p)$ is the expectation of pixel p, and $Var(A(p))$ is the true variance of the temporal amplitude of pixel p. According to the statistical theory of radar images, the temporal amplitudes in homogeneous regions obey the Rayleigh distribution. By the property that the coefficient of variation (CV) of the Rayleigh distribution is constant, for radar data with multilook L, the CV_A of the temporal amplitude can be expressed as

$$\text{CV}_A = \frac{\sqrt{\text{Var}(\cdot)}}{E(\cdot)} = \sqrt{\frac{4}{\pi} - 1}/\sqrt{L} \approx 0.52/\sqrt{L} \qquad (12)$$

where $E(\cdot)$ is the expectation. Combined with the interval estimation theory, the FaSHPS takes the average amplitude value of the reference pixel as the true value and the average amplitude value of the neighborhood pixel as the pending estimation. Then (11) is substituted as

$$P\left\{\hat{\mu}_{\text{ref}}(p) - z_{1-\alpha/2} \cdot 0.52 \cdot \hat{\mu}_{\text{ref}}(p)/\sqrt{N \cdot L} < \hat{\mu}_{\text{neig}} < \hat{\mu}_{\text{ref}}(p) \right.$$

$$\left. + z_{1-\alpha/2} \cdot 0.52 \cdot \hat{\mu}_{\text{ref}}(p)/\sqrt{N \cdot L} \right\} = 1 - \alpha \quad (13)$$

where $\hat{\mu}_{\text{ref}}(p)$ and $\hat{\mu}_{\text{neig}}$ are the average of the temporal amplitudes of the reference pixel p and its neighborhood pixels,
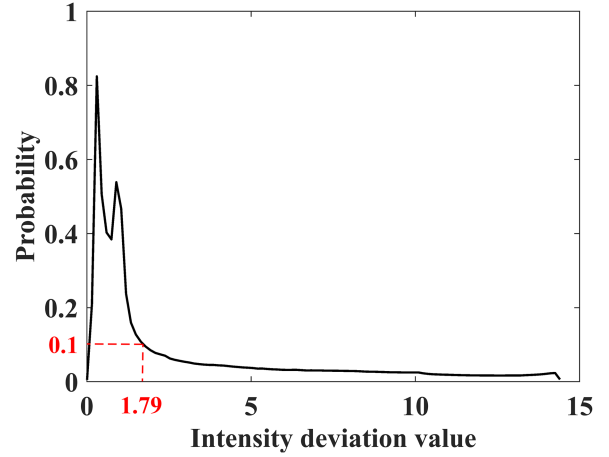

Fig. 5. Probability distribution of intensity deviation values.

respectively. If $\hat{\mu}_{\text{neig}}$ lies within the confidence interval of (13), it is considered as SHP.

Since GBR data have a shorter temporal baseline than spaceborne radar data, some noise with short time correlation will also be considered as backscatter-stabilized scatterers. In addition, the wide scanning area and complex spatial environment of the study area in this article will exacerbate the selection of noisy pixels. Considering the above actual situation, this article introduces intensity deviation, and first excludes the unstable pixels according to the intensity deviation, and then proceeds to SHPs selection. The intensity deviation D_I is

$$D_I = \frac{\sigma_I}{m_I} \qquad (14)$$

where σ_I and m_I are the standard deviation and average of the temporal intensity, respectively. The smaller the intensity deviation, the more stable the temporal backscattering of the pixel. We used a probability density function to count the probability distribution of intensity deviations in the radar data, as shown in Fig. 5. Fig. 5 shows the calculated intensity deviation values in the range 0–15. For intensity deviation values less than about 1.5, the probability is generally high, indicating that the pixels are stable in the temporal dimension, while for intensity deviation values greater than about 2, the probability is low and the curve is smooth, indicating that a small number of pixels are not stable in the temporal dimension. Unstable pixels may correspond to surface features with weak backscatter or may be noisy, which can seriously affect the accuracy of subsequent data processing. Therefore, in this article, we set the probability 0.1 as the threshold value, and pixels with probability of intensity deviation value lower than 0.1 (i.e., intensity deviation value greater than 1.79) are considered as noise and are excluded. The aim is to improve the quality of the selected SHPs.

IV. RESULTS AND DISCUSSION

A. PSs Selection Results and Analysis

In this article, the BWS test and FaSHPS are used for experiments, respectively, and the results of SHPs selection are shown in Fig. 6(a) and (c). After excluding noise pixels according to
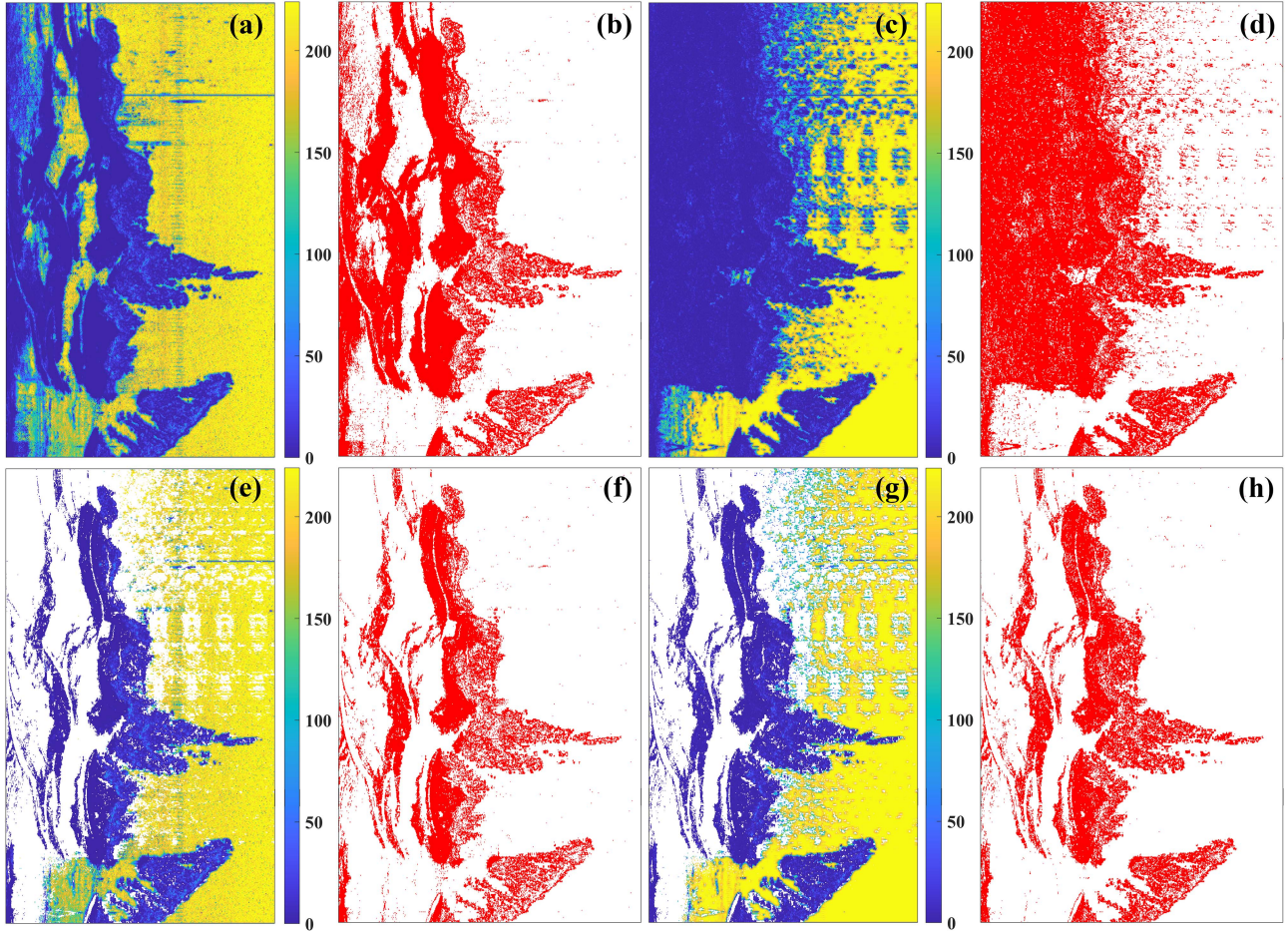
Fig. 6. Experimental results of SHPs and PSs. (a) SHPs by BWS test. (b) PSs by BWS test. (c) SHPs by FaSHPS. (d) PSs by FaSHPS. (e) SHPs by D_I + BWS. (f) PSs by D_I + BWS. (g) SHPs by D_I + FaSHPS. (h) PSs by D_I + FaSHPS.

the intensity deviation threshold, D_I + BWS and D_I + FaSHPS were used to select SHPs. The results are shown in Fig. 6(e) and (g), respectively. Fig. 6 combined with the intensity map (see Fig. 2) shows that the pixels excluded by the intensity deviation threshold are basically located in regions without backscattering or noise; the SHPs obtained by FaSHPS does not distinguish well between noisy and strongly scattering regions and are worse than the BWS test; the SHPs obtained by D_I + FaSHPS compensate well for the shortcomings of FaSHPS and do not differ significantly from D_I + BWS. Based on the number of SHPs selected, the pixels can be divided into PSs and distributed scatterers [44], [45]. Previous studies and analyses have concluded that the maximum number of SHPs considered as PSs is set to 10 [37], [40]. Therefore, in this article, pixels with the number of SHPs less than ten were selected as PSs. The results of PSs obtained from BWS test, FaSHPS, D_I + BWS, and D_I + FaSHPS are shown in Fig. 6(b), (d), (f), and (h), respectively. Furthermore, in order to compare the advantages and deficiencies of each algorithm more objectively, we have evaluated them quantitatively, as given in Table III.

Table III lists that after noise pixels are excluded by the intensity deviation threshold, the number of PSs is significantly reduced, with little difference between D_I + BWS and

TABLE III
QUANTITATIVE STATISTICAL RESULTS OF THE SHPs SELECTION ALGORITHMS

Algorithms	Number of PSs	Time consuming (s)
BWS test	857,201	30,963
FaSHPS	1,309,075	172
D_I + BWS	530,947	18,490
D_I + FaSHPS	555,112	99

D_I + FaSHPS; BWS test and D_I + BWS consume longer time, while D_I + FaSHPS has the highest computational efficiency. The above experiments show that using D_I + FaSHPS to select PSs is most appropriate. In this article, in addition to the traditional two ways of selecting PSs, the inverse of the amplitude deviation and the temporal coherence, we have combined D_I + FaSHPS to effectively enrich the selection of PSs. The experimental results show that a total of 501 877 PSs were selected for both the inverse of the amplitude deviation and the temporal coherence [see Fig. 7(a)]; 556 827 PSs were selected for both the inverse of the amplitude deviation and D_I + FaSHPS [see Fig. 7(b)]; and 771 577 PSs were selected for the inverse of the amplitude deviation, the temporal coherence, and D_I + FaSHPS [see Fig. 7(c)]. The interferometric phases
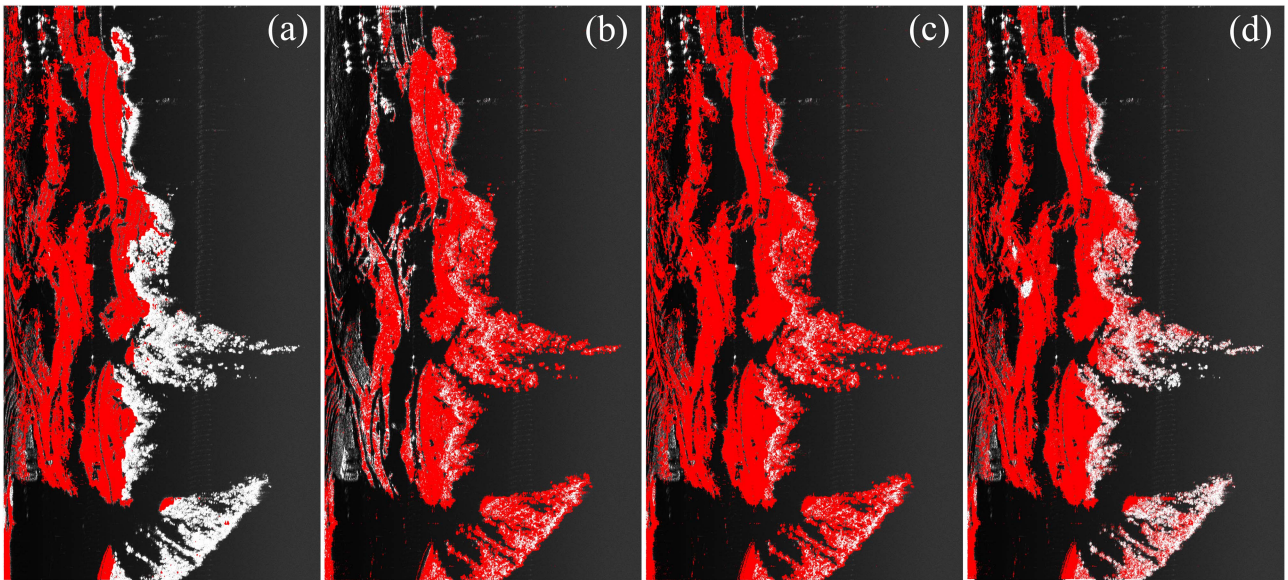
Fig. 7.   Results of PSs selection for different approaches. (a) PSs by inverse of amplitude deviation and temporal coherence. (b) PSs by inverse of amplitude deviation and D_I + FaSHPS. (c) PSs by inverse of amplitude deviation, temporal coherence, and D_I + FaSHPS. (d) Final obtained monitoring points.

of 771 577 PSs were filtered, and then a mask was set up to filter out some noisy PSs again based on indicators such as phase standard deviation and atmospheric noise, resulting in the retention of 618 173 monitoring points [see Fig. 7(d)]. The number and density of monitoring points determine whether the deformation characteristics of the study area can be reflected. Therefore, the selection of PSs considering SHPs proposed in this article not only effectively excludes the noisy points with unstable temporal scattering but also significantly increases the number and distribution density of monitoring points, which can reflect the deformation characteristics of the study area in more detail and has excellent applicability.

B. Deformation Monitoring Results and Analysis

By combining the D_I + FaSHPS algorithm with traditional PSs selection, this article uses MT-InSAR to invert the surface deformation of 618 173 monitoring points. In order to combine the analysis and discussion with the field landform, we carried out geocoding during data processing, and finally converted the deformation monitoring results from the polar coordinate system to the WGS84 geographic coordinate system for display. The LOS deformation rate calculated from 206 radar data is shown in Fig. 8. Fig. 8 shows that the overall surface deformation characteristics in the study area are stable, with deformation rates mostly in the range of −1.0–1.0 mm/d. There are several areas of significant surface deformation in the study area, which are distributed in the reservoir basin, reservoir banks, and surrounding vegetation areas of the PSPS, with a minimum deformation rate of −11.7 mm/d and a maximum rate of 11.8 mm/d.

In the reservoir basin of PSPS, the rugged ground surface and construction have resulted in some areas being decoherent and surface deformation cannot be monitored. On the reservoir banks of PSPS, where the view is open and the surface is mostly made of concrete, the coherence is higher, and thus, the monitoring

points are relatively dense and the surface deformation can be well monitored. In the vegetated areas around PSPS, the short radar wavelengths and weak penetration lead to sparse monitoring points and large fluctuations in deformation rates, which to some extent affect the accuracy of the monitoring results.

The results in Fig. 8 illustrate that we can identify the deformation areas but are not yet able to capture the surface deformation characteristics for each day of the period from 2022/07/31 10:24 to 2022/08/06 14:57. Therefore, we depict the temporal cumulative deformation of the study area, as shown in Fig. 9. The temporal figure shows that several obvious deformation areas increase in extent and magnitude with time over the monitored time period. In the study area, the maximum and minimum values of cumulative deformation are 91.3 mm and −92.9 mm, respectively.

C. Discussion of Reservoir Bank Results

Considering that the reservoir basin is the main site of construction, its surface deformation is mainly affected by construction, so it is of little significance to analyze it specifically. In addition, the vegetated areas around the PSPS are far from the center of construction operations and it is more practical to use aerial photography equipment, such as UAV, for regular inspections or manual field surveys. Therefore, this article focuses on the analysis of the deformation monitoring results of the reservoir bank. The reservoir bank has mostly been concreted and its top is relatively flat and solid, its slope is relatively steep, even nearly perpendicular to the ground in some places. Often debris and stones slip or even roll down the slope of the reservoir bank. The reservoir bank is also the area most prone to safety accidents, which can easily cause damage to workers and property. The collapse that occurred at dawn on 31 July 2022 was located in the reservoir bank [see Fig. 1(c)], which is one of the main
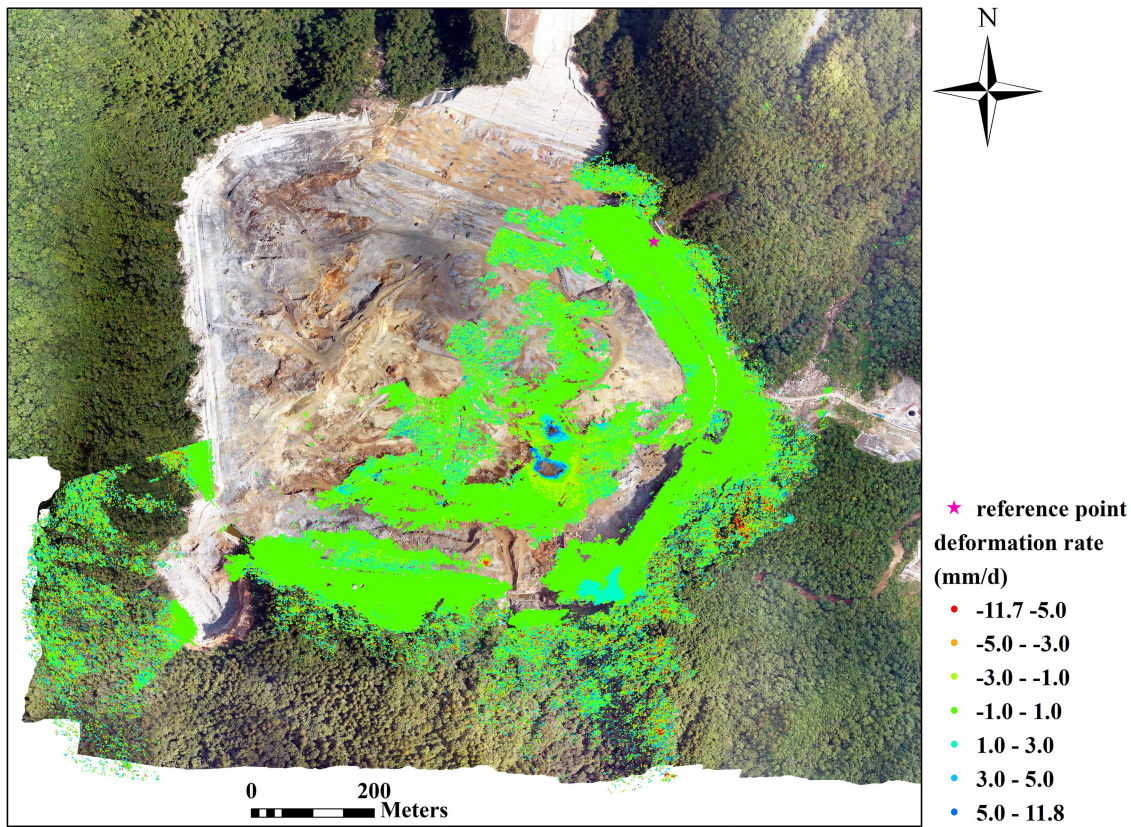
Fig. 8. Results of surface deformation rates in the study area.

reasons why this article focuses on the analysis of reservoir bank deformation.

In order to analyze the surface deformation monitoring results of the reservoir bank more clearly, we only kept the monitoring points covering the reservoir bank, as shown in Fig. 10. The deformation rate results from the reservoir bank show that there is no significant surface deformation in most areas, except for a few sporadic areas with small magnitudes of deformation. We selected five relatively obvious deformation areas for focus analysis, whose geographical location layout is shown in the black rectangle box in Fig. 10, and named them I–V. In addition, with the help of the DSM generated by the UAV images, the Areas I–V are displayed in 3-D visualization. The debris from the collapse in Area I is piled up as a slope body, with the upper part of the slope deformed more significantly and to a greater extent than the lower part. Area II is more stable overall, with deformation in some of the monitoring points at the bottom. Area III has a gentler slope and deformation is concentrated in the lower part of the slope. In Area IV, the slope is reinforced with lattice anchor retaining walls, but there is still surface deformation. Area V and Area III have similar topography, with a gentle slope and deformation sporadically distributed in the lower part of the slope. In summary, the 3-D visualization enables us to understand and study the deformation characteristics of the reservoir bank in a more intuitive and visual way.

We selected a suitable number of feature points at different geographical locations in Areas I–V. The geographical locations

and numbers of all feature points are shown in Fig. 10, and the temporal deformation trends of all feature points are depicted in Fig. 11. In addition to the statistics of deformation rate and cumulative deformation of all feature points, we also calculated the Hurst index for all feature points using the rescaled range (R/S) analysis method [46], and the results are given in Table IV. The Hurst index of the temporal deformation values lies between 0 and 1. When the Hurst index is close to 0, it means that the temporal deformation trend is weaker and may have anticontinuity; when the Hurst index is 0.5, it means that the temporal deformation trend is random; when the Hurst index is close to 1, it means that the temporal deformation trend is more continuous [47]. In Area I: the deformation trend at P1 and P2 is moderately continuous, with a cumulative deformation value of approximately 15 mm; the deformation trend at P3, P4, and P5 is less continuous, and the surface at P4 and P5 is basically stable; overall, the deformation trend gradually decreases from the top to the bottom of the collapse body. In Area II: P6–P8 are at the bottom of the reservoir bank, where the safety risk is low, and their cumulative deformation values are around 10 mm and the deformation trend in the latter days tends to be stable and not strong in continuity. In Area III: P9 has a dramatic fluctuation in deformation trend until 2022/8/3, after which the deformation trend is more or less stable; P10 has very obvious deformation at 2022/8/3 and 2022/8/4, and is relatively flat for the rest of the time; overall, the surface almost tends to stabilize. In Area IV: P11 and P12 have obvious deformation trends, with
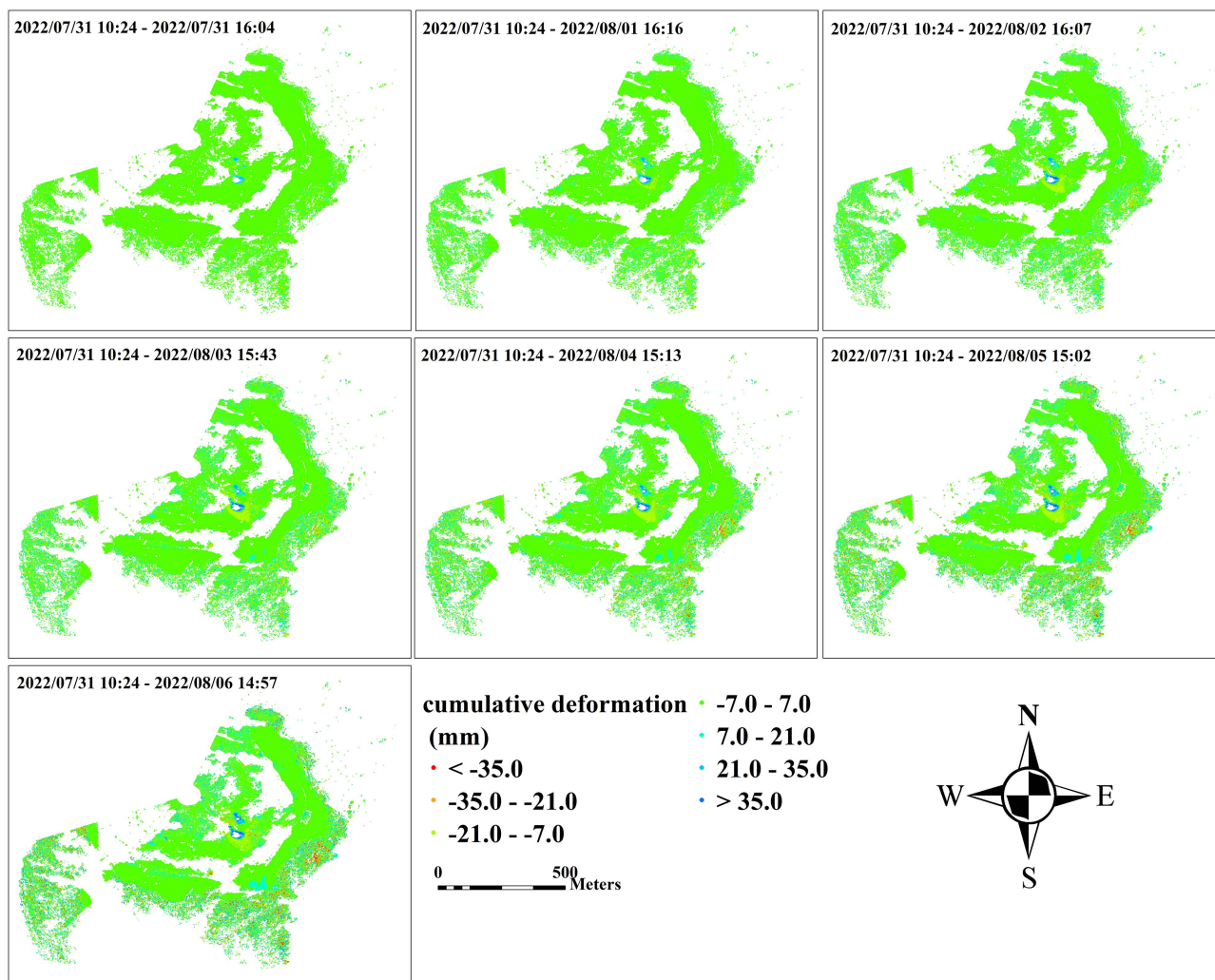
Fig. 9.   Temporal cumulative deformation in the study area.

cumulative deformation values of 49.23 mm and 33.07 mm respectively, and their Hurst indexes are greater than 0.5, at 0.60 and 0.57, respectively. It can be seen that although this area has been slope supported, there is still approximately 5 mm/d of surface movement, which is slightly continuous. Therefore, powerful measures for safety protection and focused inspection and monitoring of this area will be required in the future. In Area V: the deformation at P13 tends to converge; the deformation at P14 has an almost linear continuous trend, which requires on-site verification and protection. By analyzing the temporal deformation in Areas I–V, we can understand and grasp the deformation situation of the reservoir bank and also provide reliable data support for the relevant technical staff to identify and analyze geological hazard potential areas.

D. Deformation Factors Discussion

According to the results of the deformation rate and temporal deformation in the study area, deformation is found to occur to varying degrees in the reservoir basin, reservoir bank, and surrounding vegetation areas. The analysis of the results, combined with the field survey, revealed that the factors affecting surface deformation fall into two main categories: natural geography and man-made activities. Sudden large-scale deformation, such as collapse, is mainly influenced by natural geographical factors, while slow small-scale deformation, such as slip, is mainly influenced by man-made activities.

1) Natural Geographical Factors: The upper reservoir area is dominated by Middle Devonian strata and Indochinese intrusive granodiorite strata. The lithology of the upper section of the Middle Devonian Gudaoling Formation is mainly white and grayish marble and dark gray crystalline limestone [48]. The Indochinese intrusion lithology is gray-white granodiorite with semiautomorphic fine-grained structure and blocky tectonics. The lithology of the reservoir basin and reservoir bank is mainly crystalline limestone, and in local areas, there is a pattern of intercalation between marble and crystalline limestone, and basically no fracture structure is developed. In addition, the groundwater in the upper reservoir is mainly bedrock fracture water, with a small amount of carbonate karst fracture water locally. Fissure leakage is the main potential leakage pattern in the reservoir area. Especially in the thin parts of the mountain, in
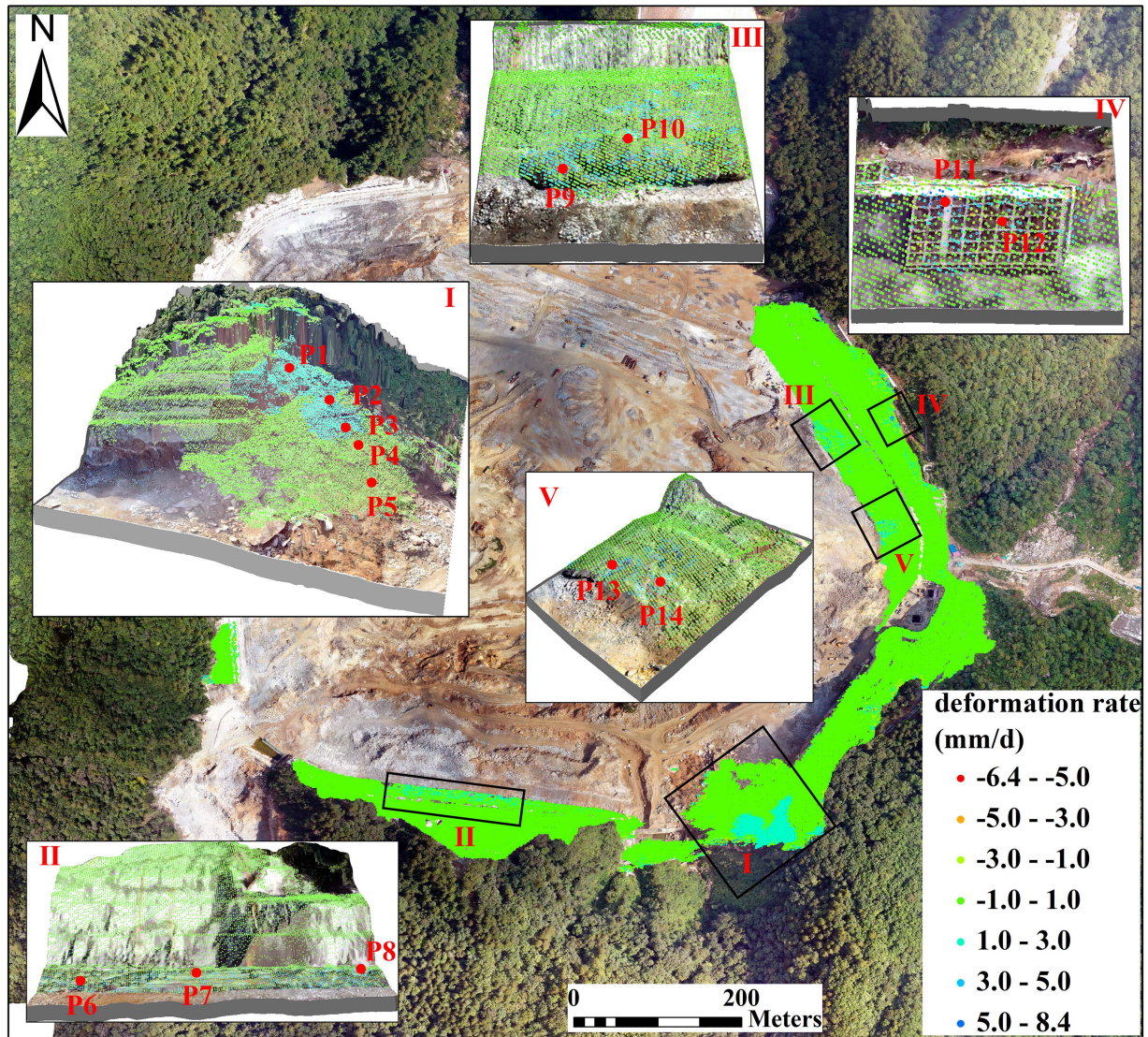
Fig. 10.   Analysis of deformation rate of the reservoir bank.

TABLE IV
STATISTICAL RESULTS OF THE TEMPORAL DEFORMATION ANALYSIS FOR ALL FEATURE POINTS

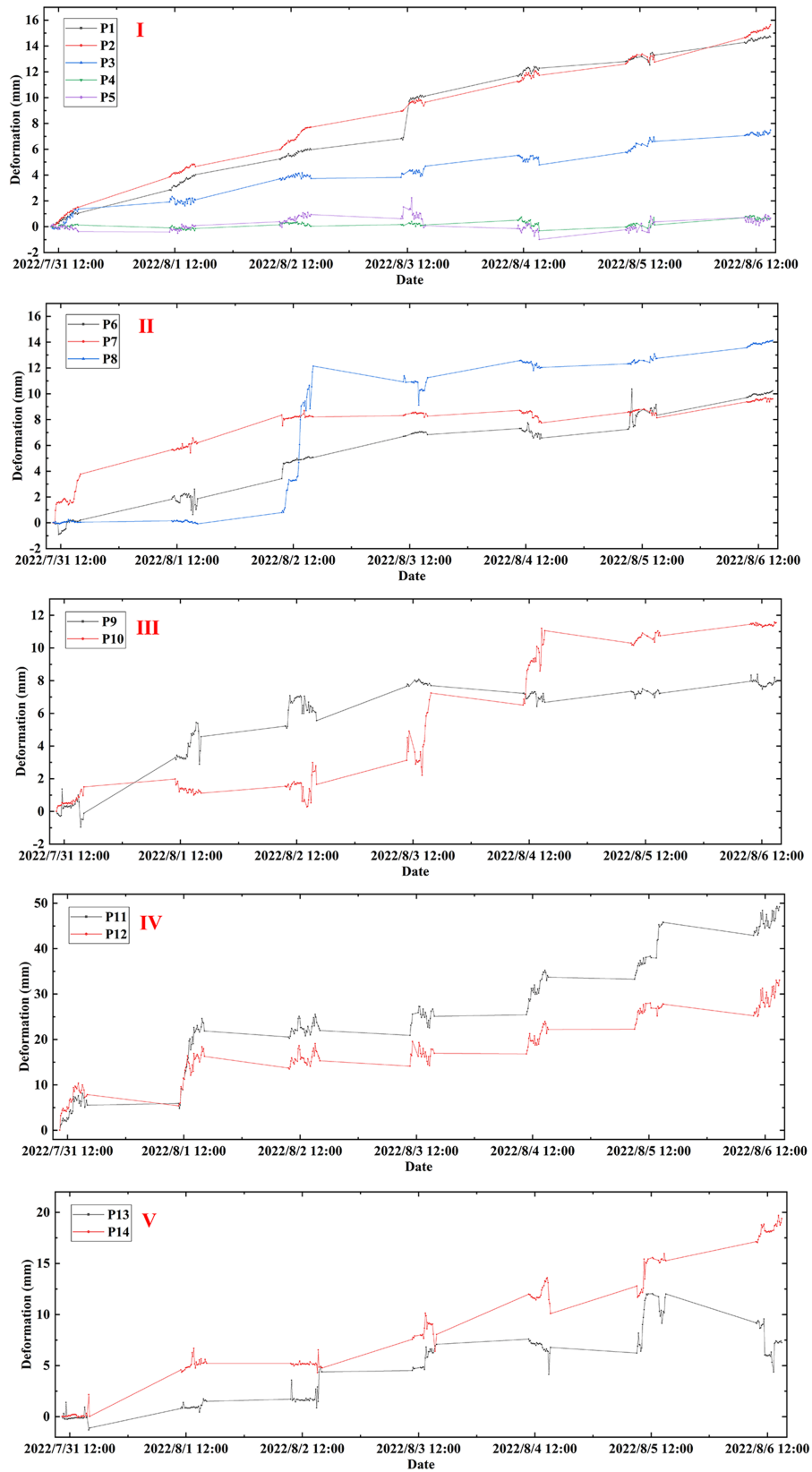| No.	Point number	Deformation rate (mm/yr)	Cumulative deformation (mm)	Hurst index
I	P1	2.19	14.71	0.55
	P2	2.35	15.64	0.57
	P3	1.10	7.50	0.49
	P4	0.09	0.65	0.45
	P5	0.05	0.67	0.47
II	P6	1.65	10.24	0.58
	P7	1.05	9.60	0.57
	P8	2.63	14.13	0.61
III	P9	1.10	7.93	0.55
	P10	2.09	11.55	0.57
IV	P11	6.40	49.23	0.60
	P12	3.48	33.07	0.57
V	P13	1.59	7.24	0.54
	P14	2.88	19.40	0.61

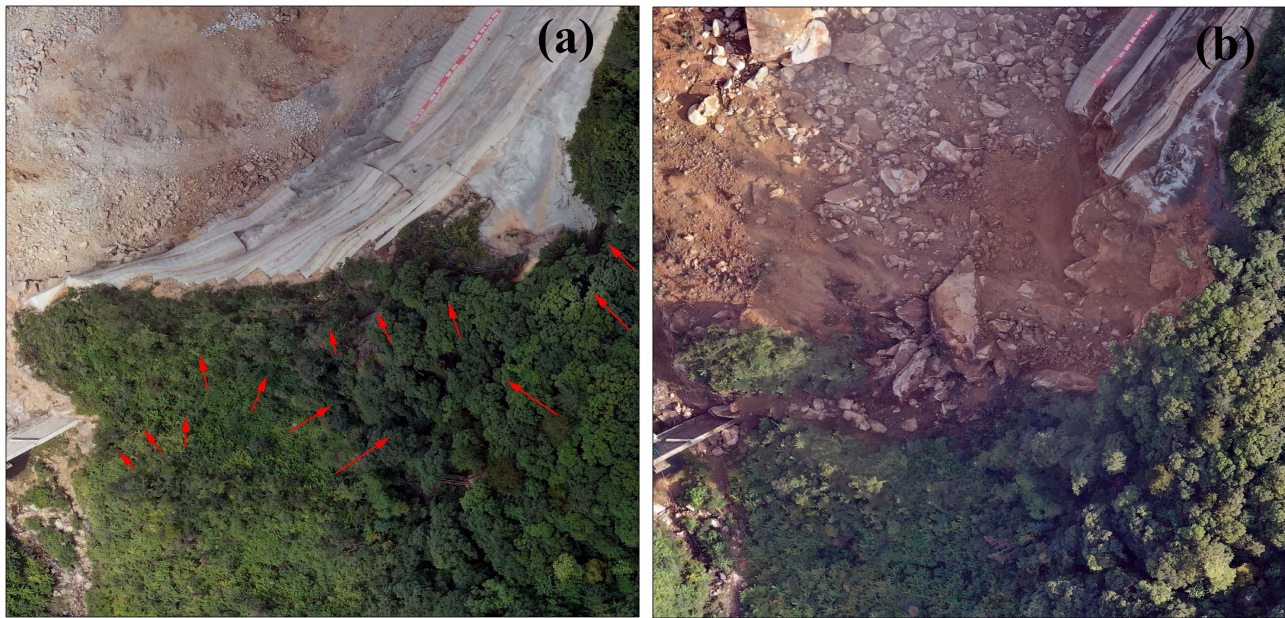Fig. 11.　Temporal deformation of feature points within Areas I–V.

Fig. 12.   (a) DOM before collapse. (b) DOM after collapse.

the pass, and in the part that runs through the adjacent valley are the locations where seepage can occur. Fortunately, through field investigation, it is found that the key areas of the reservoir bank are reinforced with concrete, and support measures are taken to minimize the influence of natural geographical factors, and the surface is basically stable.

An example is the collapse of the reservoir bank, where the collapse area is adjacent to the mountain pass in a thin area. The optical images before and after the collapse are shown in Fig. 12. In Fig. 12(a), there are some striped black voids on the back edge of the reservoir bank before the collapse, which are more similar to ground fissures. This also warns the responsible personnel to promptly identify key locations where deformation may be induced according to the natural geomorphology and geological conditions, so as to ensure that the construction of the PSPS is safe and error-free.

2) Man-Made Activity Factors: There are two main types of man-made activity factors affecting surface deformation: on-site construction and unscheduled blasting. At the upper reservoir basin, where dozens of machines, including heavy trucks and excavators, work in tandem every day; on-site photography of one moment is shown in Fig. 13(a). In the area of construction operations, the ground is accompanied by slight vibrations. In addition, there will be unscheduled blasting during the construction of PSPS in order to facilitate excavation of soil and rock. The location of the blasting during data collection was located in the southwest corner of the upper reservoir, and a distant view just after blasting is shown in Fig. 13(b). On-site verification of the areas of significant deformation based on the results of the surface deformation identification revealed that deformation of the reservoir basin was mainly caused by construction. However, deformation of the reservoir bank can be

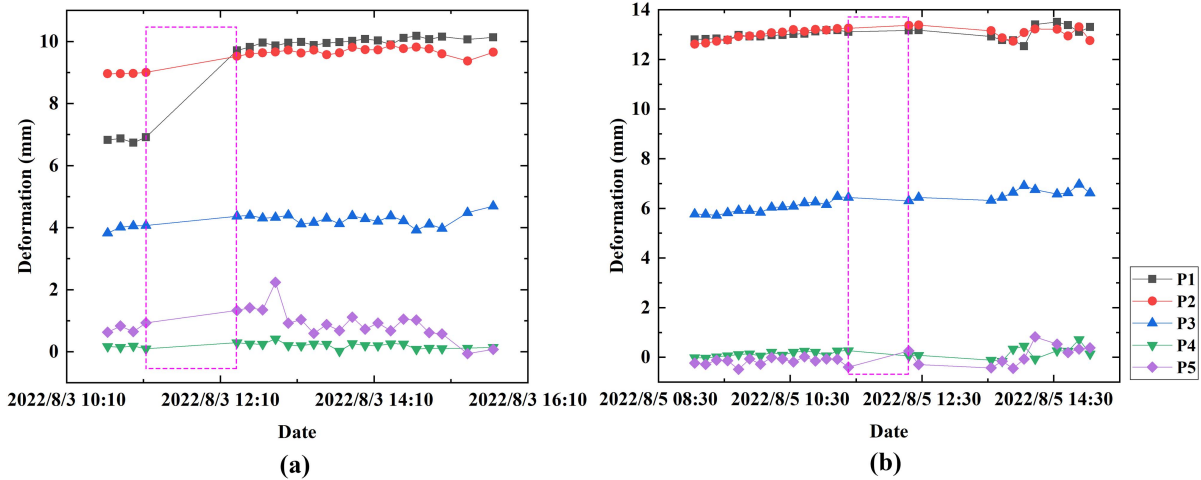Fig. 13   (a) Site construction photography. (b) Blasting remote view.

Fig. 14. Temporal deformation of P1–P5 feature points, deformation changes in the pink dotted box affected by blasting, on (a) 3 August 2022 and (b) 5 August 2022.

affected by both construction and blasting but the reservoir bank was relatively less affected by construction due to its distance from the construction site.

Two blasts occurred during the monitoring period on 3 August 2022 and 5 August 2022, respectively. In order to discuss the impact of blasting on surface stability, we take the focus Area I as an example and analyze the temporal deformation characteristics of its P1–P5 feature points in 3 August 2022 and 5 August 2022, as shown in Fig. 14. Fig. 14(a) shows that the blasting on 3 August 2022 resulted in the most obvious change in the deformation of P1 feature point, and the other feature points were also significantly affected. Fig. 14(b) shows that the effect of blasting on the deformation amplitude of each feature point on 5 August 2022 is generally less than that on 3 August 2022. This indicates that with the deposition of collapse debris over time, the surface stability is enhanced, and the influence of blasting is also reduced. Generally speaking, blasting causes short periods of ground shaking, resulting in ground deformation fluctuations, but causes little or no accelerated ground deformation over time. In addition to paying attention to the safety of personnel and equipment during blasting, the probability of secondary hazards caused by blasting is low.

V. Conclusion

This article uses the GB-InSAR technology, which has the advantage of large-angle rotational scanning to achieve surface deformation monitoring in the upper reservoir area of a PSPS in western China. We collected 206 GBR data during the monitoring time period from 2022/07/31 10:24 to 2022/08/06 14:57 and obtained temporal deformation information for the study area based on the MT-InSAR method. Some conclusions can be drawn as following.

1) In selecting PSs based on GBR data, this article takes into account information from SHPs. Based on the FaSHPS algorithm, we introduce intensity deviations to exclude pixels with unstable intensity performance in the temporal dimension and propose the D_I + FaSHPS algorithm, which has higher accuracy in the selection of SHPs and

computational efficiency. Therefore, in addition to selecting PSs using both the inverse of the amplitude deviation and the temporal coherence, this article incorporates the D_I + FaSHPS algorithm screening of PSs. Experimental results show that this not only enriches the selection method of PSs but also effectively improves the distribution density of monitoring points.

2) This article identifies several obvious deformation areas, including the collapse area, from the deformation rate and temporal deformation results. We have analyzed and discussed in detail the deformation areas, especially those located on the reservoir bank, in relation to both physical geography and man-made activities in conjunction with the on-site survey, and found that the surface is relatively stable overall, except for the effects of man-made activities. In addition, we found that there are several deformation areas on the reservoir bank that have a tendency to continue to deform and require powerful measures for safety protection and prior inspection and monitoring. Throughout the study, the GB-InSAR technology is more portable and flexible than monitoring means, such as space-borne InSAR, and has its own unique application advantages in the identification and analysis of such small-scale surface deformation in PSPS.

References

[1] Y. Kong et al., "Pumped-storage power stations in China: The past, the present, and the future," *Renew. Sustain. Energy Rev.*, vol. 71, pp. 720–731, 2017.

[2] A. Karimi, S. Heydari, F. Kouchakmohseni, and M. Naghiloo, "Scheduling and value of pumped storage hydropower plant in Iran power grid based on fuel-saving in thermal units," *J. Energy Storage*, vol. 24, 2019, Art. no. 100753.

[3] K. Ma, B. Feng, D. Zhuang, X. Guo, and Q. Gao, "Distance effects of the fault on the surrounding rock mass stability of the main powerhouse at the Huanggou pumped-storage power station," *Tunnelling Underground Space Technol.*, vol. 106, 2020, Art. no. 103568.

[4] F. Luan, B. Yuan, C. Cao, J. Yang, and Z. Xu, "Future development and features of pumped storage stations in China," in *Proc. 1st Int. Conf. Environ. Prevention Pollut. Control Technol.*, 2018, pp. 1–7.

[5] S. C. Stiros, C. Vichas, and C. Skourtis, "Landslide monitoring based on geodetically derived distance changes," *J. Surveying Eng.*, vol. 130, no. 4, pp. 156–162, 2004.

[6] C. Squarzoni, C. Delacourt, and P. Allemand, "Differential single-frequency GPS monitoring of the la Valette landslide (French alps)," *Eng. Geol.*, vol. 79, pp. 215–229, 2005.

[7] J. C. Du and H. C. Teng, "3D laser scanning and GPS technology for landslide earthwork volume estimation," *Automat. Construction*, vol. 16, pp. 657–663, 2007.

[8] G. Q. Shi et al., "Surface response and subsurface features during the restriction of groundwater exploitation in Suzhou (China) inferred from decadal SAR interferometry," *Remote Sens. Environ.*, vol. 31, 2021, Art. no. 256.

[9] H. Chen et al., "Monitoring spatiotemporal evolution of kaiyang landslides induced by phosphate mining using distributed scatterers InSAR technique," *Landslides*, vol. 20, no. 3, pp. 695–706, 2022.

[10] H. Fan et al., "Surface subsidence monitoring with an improved distributed scatterer interferometric SAR time series method in a filling mining area," *Geocarto Int.*, vol. 9, pp. 1–23, 2021.

[11] S. Selvakumaran, S. Plank, C. Geiß, C. Rossi, and C. Middleton, "Remote monitoring to predict bridge scour failure using Interferometric synthetic aperture radar (InSAR) stacking techniques," *Int. J. Appl. Earth Observation Geoinf.*, vol. 73, pp. 463–470, 2018.

[12] Z. Wang, Z. Li, Y. Liu, J. Peng, S. Long, and J. Mills, "A new processing chain for real-time ground-based SAR (RT-GBSAR) deformation monitoring," *Remote Sens.*, vol. 11, 2019, Art. no. 2437.

[13] J. Han, H. Yang, Y. Liu, Z. Lu, K. Zeng, and R. Jiao, "A deep learning application for deformation prediction from ground-based InSAR," *Remote Sens.*, vol. 14, 2022, Art. no. 5067.

[14] G. Luzi et al., "Ground-based radar interferometry for landslides monitoring: Atmospheric and instrumental decorrelation sources on experimental data," *IEEE Trans. Geosci. Remote Sens.*, vol. 42, no. 11, pp. 2454–2466, Nov. 2004.

[15] S. Rodelsperger and A. Meta, "MetaSensing's FastGBSAR: Ground based radar for deformation monitoring," in *Proc. SAR Image Anal., Model., Techn. XIV, Int. Soc. Opt. Photon.*, 2014, Art. no. 924318.

[16] C. Werner, T. Strozzi, A. Wiesmann, and U. Wegmuller, "A real-aperture radar for ground-based differential interferometry," in *Proc. IEEE Int. Geosci. Remote Sens. Symp.*, 2008, pp. III-210–III-213.

[17] T. Carlà et al., "Combination of GNSS, satellite InSAR, and GBInSAR remote sensing monitoring to improve the understanding of a large landslide in high alpine environment," *Geomorphology*, vol. 335, pp. 62–75, 2019.

[18] M. Pieraccini and L. Miccinesi, "Ground-based radar interferometry: A bibliographic review," *Remote Sens.*, vol. 11, 2019, Art. no. 1029.

[19] A. Woods et al., "GB-InSAR monitoring of vegetated and snow-covered slopes in remote mountainous environments," *Landslides*, vol. 17, pp. 1713–1726, 2020.

[20] D. Traglia et al., "Tracking morphological changes and slope instability using spaceborne and ground-based SAR data," *Geomorphology*, vol. 300, pp. 95–112, 2018.

[21] D. Tapete, N. Casagli, G. Luzi, R. Fanti, G. Gigli, and D. Leva, "Integrating radar and laser-based remote sensing techniques for monitoring structural deformation of archaeological monuments," *J. Arch. Sci.*, vol. 40, no. 1, pp. 176–189, 2013.

[22] A. Serrano-Juan et al., "Gb-sar interferometry displacement measurements during dewatering in construction works case of Lasagrera railway station in Barcelona, Spain," *Eng. Geol.*, vol. 205, no. 29, pp. 104–115, 2016.

[23] C. Gentile and G. Bernardini, "An interferometric radar for non-contact measurement of deflections on civil engineering structures: Laboratory and full-scale tests," *Struct. Infrastruct. Eng.*, vol. 6, no. 5, pp. 521–534, 2010.

[24] A. Hooper, "A multi-temporal InSAR method incorporating both persistent scatterer and small baseline approaches," *Geophys. Res. Lett.*, vol. 35, no.no. 16, 2008, Art. no. L16302.

[25] A. Ferretti, C. Prati, and F. Rocca, "Permanent scatterers in SAR interferometry," *IEEE Trans. Geosci. Remote Sens.*, vol. 39, no. 1, pp. 8–20, Jan. 2001.

[26] P. Berardino, G. Fornaro, R. Lanari, and E. Sansosti, "A new algorithm for surface deformation monitoring based on small baseline differential SAR interferograms," *IEEE Trans. Geosci. Remote Sens.*, vol. 40, no. 11, pp. 2375–2383, Nov. 2002.

[27] A. Hooper, D. Bekaert, K. Spaans, and M. Arıkan, "Recent advances in SAR interferometry time series analysis for measuring crustal deformation," *Tectonophysics*, vol. 514, pp. 1–13, 2012.

[28] J. Hu et al., "Resolving three-dimensional surface displacements from InSAR measurements: A review," *Earth Sci. Rev.*, vol. 133, pp. 1–17, 2014.

[29] N. Casagli et al., "Spaceborne, UAV and ground-based remote sensing techniques for landslide mapping, monitoring and early warning," *Geoenviron. Disasters*, vol. 4, no. 1, pp. 1–23, 2017.

[30] J. Dong et al., "Mapping landslide surface displacements with time series SAR interferometry by combining persistent and distributed scatterers: A case study of Jiaju landslide in Danba, China," *Remote Sens. Environ.*, vol. 205, pp. 180–198, 2018.

[31] D. Perissin and T. Wang, "Time-series InSAR applications over urban areas in China," *IEEE J. Sel. Topics Appl. Earth Observ. Remote Sens.*, vol. 4, no. 1, pp. 92–100, Jan. 2010.

[32] R. Iglesias, J. J. Mallorqui, and P. López-Dekker, "DInSAR pixel selection based on sublook spectral correlation along time," *IEEE Trans. Geosci. Remote Sens.*, vol. 52, no. 7, pp. 3788–3799, Jul. 2013.

[33] A. Ferretti, A. Fumagalli, F. Novali, C. Prati, F. Rocca, and A. Rucci, "A new algorithm for processing interferometric data-stacks: SqueeSAR," *IEEE Trans. Geosci. Remote Sens.*, vol. 49, no. 9, pp. 3460–3470, Sep. 2011.

[34] M. Jiang, X. Ding, R. F. Hanssen, R. Malhotra, and L. Chang, "Fast statistically homogeneous pixel selection for covariance matrix estimation for multitemporal InSAR," *IEEE Trans. Geosci. Remote Sens.*, vol. 53, no. 3, pp. 1213–1224, Mar. 2015.

[35] W. Kössler, "Max-type rank tests, U-tests, and adaptive tests for the two-sample location problem—An asymptotic power study," *Comput. Statist. Data Anal.*, vol. 54, no. 9, pp. 2053–2065, 2010.

[36] A. Parizzi and R. Brcic, "Adaptive InSAR stack multilooking exploiting amplitude statistics: A comparison between different techniques and practical results," *IEEE Geosci. Remote Sens. Lett.*, vol. 8, no. 3, pp. 441–445, May 2011.

[37] Z. Wang, Z. Li, and J. P. Mills, "A new nonlocal method for ground-based synthetic aperture radar deformation monitoring," *IEEE J. Sel. Topics Appl. Earth Observ. Remote Sens.*, vol. 11, no.no. 10, pp. 3769–3781, Oct. 2018.

[38] Z. Z. Shen, L. Zhang, and L. Q. Xu, "Optimization of seepage prevention form of the zhen'an pumped storage power station," *Appl. Mechanics Mater.*, vol. 724, pp. 180–184, 2015.

[39] Y. Su et al., "A novel near-real-time GB-InSAR slope deformation monitoring method," *Remote Sens.*, vol. 14, 2022, Art. no. 5585.

[40] K. Spaans and A. Hooper, "InSAR processing for volcano monitoring and other near-real time applications," *J. Geophys. Res. Solid Earth*, vol. 121, pp. 2947–2960, 2016.

[41] Z. Wang, Z. Li, and J. Mills, "A new approach to selecting coherent pixels for ground-based SAR deformation monitoring," *ISPRS J. Photogrammetry Remote Sens.*, vol. 144, pp. 412–422, 2018.

[42] S. Li, W. Xu, and Z. Li, "Review of the SBAS InSAR Time-series algorithms, applications, and challenges," *Geodesy Geodyn.*, vol. 13, no. 2, pp. 114–126, 2022.

[43] W. Baumgartner, P. Weiß, and H. Schindler, "A nonparametric test for the general two-sample problem," *Biometrics*, vol. 9, pp. 1129–1135, 1998.

[44] F. Zhao and J. J. Mallorqui, "SMF-POLOPT: An Adaptive multitemporal Pol(DIn)SAR filtering and phase optimization algorithm for PSI applications," *IEEE Trans. Geosci. Remote Sens.*, vol. 57, no. 9, pp. 7135–7147, Sep. 2019.

[45] Y. Liu, H. Yang, J. Fan, J. Han, and Z. Lu, "NL-MMSE: A hybrid phase optimization method in multimaster interferogram stack for DS-InSAR applications," *IEEE J. Sel. Topics Appl. Earth Observ. Remote Sens.*, vol. 15, pp. 8332–8345, 2022.

[46] H. E. Hurst, "Long-term storage capacity of reservoirs," *Trans. Amer. Soc. Civil Eng.*, vol. 116, pp. 770–799, 1951.

[47] Y. Liu, H. Yang, S. Wang, L. Xu, and J. Peng, "Monitoring and stability analysis of the deformation in the Woda landslide area in Tibet, China by the DS-InSAR method," *Remote Sens.*, vol. 14, 2022, Art. no. 532.

[48] H. Z. Li et al., "Geochemical characteristics and their geological implication of Cherts from Bafangshan-Erlihe area in western Qinling Orogen," *Acta Petrological Sinica*, vol. 25, no. 11, pp. 3094–3102, 2009.

Honglei Yang was born in February 1983. He received the Ph.D. degree in cartography and geographical information engineering from the China University of Geosciences, Beijing, China, in 2012.

Since 2014, he has been teaching at the China University of Geosciences, where he currently serves as a Professor and Ph.D. Supervisor. He has presided over and participated in the projects of the National Natural Science Foundation of China, the Key Research and Development Program of the Ministry of Science and Technology, and the China–Europe Dragon Project. He has authored or coauthored more than 30 papers. He is involved in scientific research in the fields of satellite and ground-based InSAR data processing, microwave remote sensing data processing theory and applications, etc.

Yuhan Su is currently working toward the Ph.D. degree with the School of Land Science and Technology, China University of Geosciences, Beijing, China.

His research interests include interferometric synthetic aperture radar data processing methods and their applications in natural hazard.

Youfeng Liu received the B.S. degree in surveying and mapping engineering from Henan Polytechnic University, Jiaozuo, China, in 2018 and the M.S. degree in Geodesy from the China University of Mining and Technology, Xuzhou, China, in 2021. He is currently working toward the Ph.D. degree with the School of Land Science and Technology, China University of Geosciences, Beijing, China.

His research interests include satellite and ground-based InSAR data processing and its application in surface deformation monitoring.

Xu Ma received the B.S. degree in surveying engineering from the Nanjing University of Information Science and Technology, Nanjing, China, in 2017, and the M.S. degree in surveying and mapping from the China University of Mining and Technology, Beijing, China, in 2020. He is currently working toward the Ph.D. degree in InSAR data processing and geohazard monitoring with the China University of Geosciences, Beijing, China.

Hongdong Fan received the Ph.D. degree from the China University of Mining and Technology, Xuzhou, China, in 2010.

He is currently an Associate Professor with the School of Environment and Spatial Informatics, China University of Mining and Technology. He has authored or coauthored more than 30 peer-reviewed articles in journals, such as IEEE TRANSACTIONS ON GEOSCIENCE AND REMOTE SENSING, *IEEE Geoscience and Remote Sensing Letters*, and *International Journal of Applied Earth Observation and Geoinformation*. His research interests include geohazard prevention and deformation monitoring.

Liuyu Wang received the B.S. degree in surveying and mapping engineering and the Ph.D. degree in geodesy and survey engineering, both from the China University of Mining and Technology, Xuzhou, China, in 2014 and 2020, respectively.

Her research focuses on time-series InSAR analysis and deformation monitoring.

Xiaoliang Li received the B.S. degree in engineering surveying and mapping from Hohai University, Nanjing, China, in 2004 and the M.S. degree in survey and mapping from the China University of Geosciences, , Beijing, China, in 2015.

He is currently a Senior Engineer with the Beijing Institute of Surveying and Mapping, Beijing. His research interests include geohazard prevention and deformation monitoring.